ELSEVIER

Characterization of crystalline structure of ball-milled nano-Ni–Zn-ferrite by Rietveld method

S. Bid, S.K. Pradhan*

Department of Physics, The University of Burdwan, Golapbag, Burdwan 713104, West Bengal, India

Abstract

Nanocrystalline Ni–Zn-ferrite is synthesized at room temperature by high-energy ball milling with the target composition 0.5 ZnO, 0.5 NiO and 1.0 α-Fe_2O_3 ((0.5 + 0.5):1 mole fraction). The formation of non-stoichiometric ferrite phase is noticed after 1 h of ball milling and its content increases with increasing milling time. The structural and microstructural evolution of nickel–zinc-ferrite caused by milling is investigated by X-ray powder diffraction. The relative phase abundances of different phases, particle size, r.m.s. (root mean square) strain, lattice parameter change, etc. have been estimated from Rietveld's powder structure refinement analysis of XRD data. It is revealed from the XRD pattern that ZnO reflections are completely disappeared within 1 h of milling but a significant amount ($\sim$7 wt.%) of nanocrystalline NiO and α-Fe_2O_3 ($\sim$12 wt.%) remain excess even after 11 h of milling. It indicates that during ball milling a non-stoichiometric mixture of NiO, ZnO and α-Fe_2O_3 may lead to the formation of non-stoichiometric Ni–Zn-ferrite. A considerable amount of ferrite is formed within 11 h of ball milling with lattice parameter higher than that of stoichiometric Ni–Zn-ferrite prepared by conventional ceramic route keeping the same powder mixture at 1473 K for 2 h. The 11 h milled sample is post-annealed at 773 K for different durations to verify the solubility of both the residual parts of NiO and α-Fe_2O_3 in forming the target composition. The post-annealing treatment reveals that within 1 h of post-annealing, stoichiometric Ni–Zn-ferrite is formed and nanocrystalline ferrite particles become almost strain-free within 15 h of post-annealing time.
© 2003 Elsevier B.V. All rights reserved.

Keywords: Nanocrystalline Ni–Zn-ferrite; Ball milling; Rietveld's method

1. Introduction

The synthesis of nanocrystalline spinel Ni–Zn-ferrites has been investigated intensively in recent years due to their potential applications in non-resonant devices, radio frequency circuits, high-quality filters, rod antennas, transformer cores, read/write heads for high-speed digital tapes and operating devices [1–3]. Nowadays, these materials are largely synthesized in nanometric scale for new and improvised properties [4–6]. Nanometric $Ni_{1-x}Zn_x$ ferrites show good dielectric properties [7] and high performance [8] at relatively low sintering temperature. Among the other methods of preparation of nanocrystalline powders, high-energy milling is a very suitable solid-state processing technique for the preparation of nanocrystalline ferrite powders exhibiting new and unusual properties [9–12]. Reports on synthesis of nanocrystalline Ni–Zn-ferrites by high-energy ball milling of stoichiometric NiO, ZnO and α-Fe_2O_3 mixture are not found in the literature. To the best of our knowledge, so far the microstructure characterization

and phase transformation kinetics of ball mill prepared Ni–Zn-ferrites have not been studied yet in detail by X-ray powder structure refinement method.

The crystalline Ni–Zn-ferrite (cubic, $a = 0.8399$ nm, space group: Fd$\bar{3}$m, $Z = 8$; ICDD PDF #08-0234) is a normal spinel at room temperature. Spinel structure is known by the general formula AB_2O_4, consisting of an almost perfect interstices cubic closed-packed oxygen arrangement, in which the cations reside on tetrahedral (A) and octahedral [B] sites. The structural formula of a ferrite is usually written as $(X_{1-\delta}^{2+}Y_\delta^{3+})[X_\delta^{2+}Y_{2-\delta}^{3+}]O_4^{2-}$, where round and square brackets denote sites of tetrahedral (A) and octahedral [B] coordination, respectively, and δ represents the degree of inversion (defined by the fraction of the A sites occupied by Y^{3+} cations). The completely random distribution of A and B cations over the three cation sites corresponds to mixed spinel configuration which is asymptotically approached at very high temperatures [13]. Same type of cation distribution is also observed in ball-milled samples [9,14]. The change in temperature or the change in milling parameter may result in change in the degree of inversion. The Ni–Zn-ferrite is a soft magnetic ceramic that has spinel configuration of the type $(Zn_{1-x}Fe_x)[Ni_xFe_{2-x}]O_4$. In this

* Corresponding author. Fax: +91-342-530452.
E-mail address: skpdn@vsnl.net (S.K. Pradhan).

formula the metallic cations Fe^{3+}/Zn^{2+} occupy the tetrahedral A sites and the metallic cations Fe^{3+}/Ni^{2+} occupy the octahedral B sites [15].

High-energy ball milling has now become one of the conventional methods for production of nano-/non-crystalline materials. During the ball milling, materials in powder form suffer severe high-energy impacts in the process of ball-to-ball and ball-to-vial wall collisions of the grinding media. Formation of nanocrystalline materials in the process of ball milling usually caused by the continuous fragmentation and re-welding mechanism of grains. The process sometimes leads to several polymorphic phase transformations that are reasoned by the formation of huge amount of structural and microstructural defects. It is therefore necessary to characterize these defect states of the ball-milled material in order to find the reason for phase transformation. Physical properties of a material depend upon the microstructures and therefore by controlling the microstructure, materials can be designed according to desirable properties. The powder patterns of almost all the ball-milled materials, milled at different milling time are composed of a large number of overlapping reflections of α-Fe_2O_3, NiO, ZnO and Ni–Zn-ferrite phases [10–12,14]. Rietveld's analysis based on structure and microstructure refinement [16,17] has been adopted in the present analysis for precise determination of several microstructural parameters as well as relative phase abundance of such multiphase material containing a large number of overlapping reflections. The purposes of our present work are: (i) to prepare nanocrystalline Ni–Zn-ferrite phase by high-energy ball milling the stoichiometric mixture (1:1 mol%) of powdered reactants containing 67.17, 15.71 and 17.11 wt.% of α-Fe_2O_3, NiO and ZnO phases, respectively, at room temperature; (ii) to study the phase transformation kinetics of the ball-milled mixture; (iii) to determine the relative phase abundances of different structures and to characterize prepared materials in terms of several microstructural defect parameters (change in lattice parameter, atomic position, particle size, r.m.s. lattice strains, etc.) employing Rietveld's powder structure refinement method [16,18–21].

2. Experimental

Accurately weighed powders of 17.5 wt.% ZnO (M/s Merck, 99% purity), 15.7 wt.% NiO (M/s Merck, 99% purity) and 66.8 wt.% α-Fe_2O_3 (M/s Glaxo, 99% purity) were hand-ground in an agate mortar under doubly distilled acetone for more than 5 h for a homogeneous mixture of the powders. High-energy ball milling of a part of the dried homogeneous powder mixture was conducted in a planetary ball mill (Model P5, M/s Fritsch, GmbH, Germany). In a planetary ball mill, a rotating disk carries vials that rotate in opposite direction. The rotation speed of the disk was 325 rpm and that of the vials was about 475 rpm. Milling of powder samples was done at room temperature in hardened

chrome steel (Fe–1 wt.% Cr) vial (volume 80 ml) using 30 hardened chrome steel balls of 10 mm diameter at BPMR = 40:1. The time of milling varies from 1 to 11 h depending upon the rate of formation of Ni–Zn-ferrite phase.

The X-ray powder diffraction profiles of the unmilled homogeneous powder mixture, ball-milled and post-annealed samples were recorded using Ni-filtered Cu Kα radiation from a highly stabilized and automated Philips X-ray generator (PW 1830) operated at 35 kV and 25 mA. The generator is coupled with a Philips X-ray powder diffractometer consisting of a PW 3710 mpd controller, PW 1050/37 goniometer, and a proportional counter. For this experiment, $1°$ divergence slit, 0.2 mm receiving slit, $1°$ scatter slit were used. The step-scan data (of step size $2\theta = 0.02°$ and counting time 5 s) for the entire angular range ($2\theta = 15–80°$) of the experimental samples were recorded and stored in a PC, coupled with the diffractometer. Post-annealing of the 11 h ball-milled sample was conducted at 773 K for 1, 4, 7, 10 and 15 h in a programmable furnace (M/s Thermolyne, USA).

3. Method of analysis

In the present study, we have adopted the Rietveld's powder structure refinement analysis [16,18–21] of X-ray powder diffraction data to obtain the refined structural parameters, such as atomic coordinates, occupancies, lattice parameters, thermal parameters, etc. and microstructural parameters, such as particle size and r.m.s. lattice strain, etc. For instrumental broadening correction a specially processed Si standard [22] was used. The resolving of (1 1 1) reflection of Si at even $2\theta \sim 28.4°$ into Kα_1 and Kα_2 components indicates that the instrumental broadening is very small. However, U, V, W coefficients from $(FWHM)^2$ versus $\tan\theta$ variations (varies non-linearly with increasing scattering angle) were estimated and incorporated in the Rietveld's software as instrumental broadening. The Rietveld's software MAUD 1.85 [17] is specially designed to refine simultaneously both the structural and microstructural parameters through a least-squares method. The peak shape was assumed to be a pseudo-Voigt (pV) function with asymmetry. The background of each pattern was fitted by a polynomial function of degree 4. In the present study, refinements were conducted without refining the isotropic atomic thermal parameters.

To simulate the theoretical X-ray powder diffraction pattern containing all the ZnO, NiO, α-Fe_2O_3, Ni–Zn-ferrite (normal spinel) phases in a single pattern the following considerations were made:

(i) For ZnO (hexagonal), the space group was taken as P6$_3$mc with all atoms in general Wyckoff position 2(b).
(ii) For NiO (cubic), the space group was taken as Fm$\bar{3}$m, with Ni and O atoms in special Wyckoff positions 4(a) and 4(b), respectively.

(iii) For α-Fe_2O_3 (rhombohedral), the space group was taken as $R\bar{3}c$, with Fe and O atoms in special Wyckoff positions 12(c) and 18(e), respectively.

(iv) For Ni–Zn-ferrite (cubic, normal spinel) the space group was taken as $Fd\bar{3}m$ with Ni and Zn atom in the special Wyckoff positions 8(f) and Fe and O in the 16(c) and 32(b), respectively.

3.1. Crystalline structure characterization by X-ray powder diffraction

For microstructure characterization the experimental profiles were fitted with the most suitable pV analytical function [20] because it takes individual care for both the particle size and strain broadening of the experimental profiles.

For both the $K\alpha_1$ and $K\alpha_2$ profiles, the line broadening function $B(2\theta)$ and the symmetric part of instrumental function $S(2\theta)$ may be represented by the pV function [20]:

$$pV(x) = \sum_{\alpha_1 \alpha_2} I_{nt}[\eta C(x) + (1 - \eta)G(x)] \tag{1}$$

where the Cauchyian component, $C(x) = (1 + x^2)^{-1}$ and the Gaussian component, $G(x) = \exp[-(\ln 2)x^2]$ with $x = (2\theta - 2\theta_0)/HWHM$ (HWHM is the half width at half maxima of the X-ray peaks) and $HWHM = (1/2)FWHM = (1/2)(U \tan^2 \theta + V \tan \theta + W)^{1/2}$, where U, V and W are coefficients of the quadratic polynomial, η is the Gaussianity of X-ray profile, θ_0 the Bragg angle of $K\alpha_1$ peak and I_{nt} is the scale factor.

The powder diffraction patterns were simulated providing all necessary structural information and some starting values of microstructural parameters of the individual phases with the help of the Rietveld's software, the MAUD 1.85 [17]. Initially, the positions of the peaks were corrected by successive refinements of zero-shift error. Considering the integrated intensity of the peaks as a function of structural parameters only, the Marquardt least-squares procedures were adopted for minimization the difference between the observed and simulated powder diffraction patterns and the minimization was carried out by using the reliability index parameter, R_{wp} (weighted residual error), and R_B (Bragg factor) defined as

$$R_{wp} = \left[\frac{\sum_i w_i(I_0 - I_c)^2}{\sum_i w_i I_0^2} \right]^{1/2} \tag{2}$$

and

$$R_B = \frac{100 \sum |I_0 - I_c|}{\sum I_0} \tag{3}$$

The goodness of fit (GoF) is established by comparing R_{wp} with the expected error, R_{exp}

$$R_{exp} = \left[\frac{N - P}{\sum_i w_i I_0^2} \right]^{1/2} \tag{4}$$

where I_0 and I_c are the experimental and calculated intensities, respectively, w_i ($=1/I_0$) and N are the weight and number of experimental observations, and P the number of fitting parameters. This leads to the value of GoF [16,17,21]:

$$GoF = \frac{R_{wp}}{R_{exp}} \tag{5}$$

Refinement continues till convergence is reached with the value of the quality factor, GoF very close to 1 (varies between 1.07 and 1.25), which confirms the goodness of refinement.

The Rietveld's method was successfully applied for determination of the quantitative phase abundances of the composite materials [23–26]. There is a simple relationship between the individual scale factor determined, considering all refined structural parameters of individual phases of a multiphase sample, and the phase concentration (volume/weight fraction) in the mixture. The weight fraction (W_i) for each phase was obtained from the refinement relation:

$$W_i = \frac{S_i(ZMV)_i}{\sum_j S_j(ZMV)_j} \tag{6}$$

where i is the value of j for a particular phase among the N phases present, S_j the refined scale factor, Z the number of formula units per cell, M the atomic weight of the formula unit and V the volume of the unit cell [16,17]. The structure refinement along with size-strain broadening analysis was carried out simultaneously by adopting the standard procedure [16,17].

3.2. Size-strain analysis

The basic consideration of this method is the modeling of the diffraction profiles by an analytical function, which is a combination of Cauchyian, Gaussian, and asymmetry functions as well. It has been well established that the observed peak-broadenings of the sample profiles are mainly due to the presence of small particle size and r.m.s. strain inside the particles. The particle size and strain broadening can be approximated better with Cauchy and Gaussian type functions, respectively [27,28]. Being a linear combination of a Cauchyian and Gaussian functions, the pV function is the most reliable peak-shape function and is being widely used in the Rietveld's structure refinement software.

The process of successive profile refinements modulated different structural and microstructural parameters of the simulated pattern to fit the experimental diffraction pattern. Profile refinement continues until convergence is reached in each case, with the value of the quality factor (GoF) approaches very close to 1.

4. Results and discussion

The XRD powder patterns recorded from unmilled and ball-milled (BPMR = 40:1) homogeneous powder mixtures
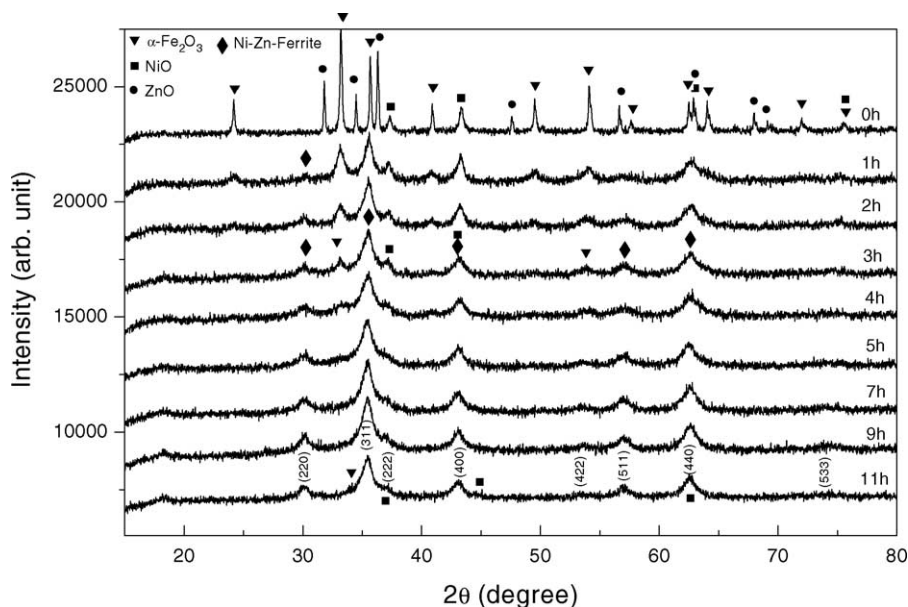
Fig. 1. X-ray powder diffraction patterns of unmilled and ball-milled (NiO + ZnO)-α-Fe$_2$O$_3$ mixture (1:1 mol%) at BPMR 40:1. Only Ni–Zn-ferrite reflections have been indexed.

are shown in Fig. 1. The powder pattern of unmilled mixture contains only the individual reflections of NiO (ICDD PDF #04-0835), ZnO (ICDD PDF #36-1451), and α-Fe$_2$O$_3$ (ICDD PDF #33-0664) phases only. It is evident from the figure that in the course of ball milling the NiO, ZnO and α-Fe$_2$O$_3$ mixture, the Ni–Zn-ferrite phase has been formed and its amount increases gradually with increasing milling time. After just 1 h of milling, the formation of Ni–Zn-ferrite phase has been noticed clearly due to the appearance of at least (2 2 0) (isolated, $2\theta = 30.13°$) and most strongest (3 1 1) (overlapped, $2\theta = 35.43°$) reflections in the respective XRD pattern. It is also evident from the figure that the content of ZnO phase has been reduced to a large extent in comparison to NiO and α-Fe$_2$O$_3$ phase and vanishes within 1 h of ball-milling. It indicates that the ZnO phase is much prone to deformation fault as all the reflections are sufficiently broadened in comparison to other two phases and rate of solid-state diffusion of ZnO into the α-Fe$_2$O$_3$ lattice is higher than NiO phase. It seems that initially Zn-ferrite phase is formed from the ZnO-α-Fe$_2$O$_3$ solid solution. A small amount of Ni–Zn-ferrite is formed when the NiO phase diffuses slowly into the ZnFe$_2$O$_4$ lattice in the course of milling. It has been reported earlier by ourselves [24] the formation of ZnFe$_2$O$_4$ within 30 min of ball milling the homogeneous stoichiometric (1:1 mol%) powder mixture of ZnO and α-Fe$_2$O$_3$ phases using the same experimental setup. In the course of milling, all the reflections of ferrite phase appear distinctly with sufficient peak-broadening in the XRD pattern of 3 h ball-milled sample. At the same time, intensities of starting materials have been reduced further and except the strongest (1 0 4) ($2\theta = 33.18°$) reflection of α-Fe$_2$O$_3$ phase all other reflections are apparently disappeared. It indicates that: (i) contents of the staring phases

have been reduced considerably within this time of milling, (ii) peak-broadening increases significantly because the nanocrystalline particles contains a huge amount of lattice strain arising from high-energy milling. As some of the reflections are overlapped with very broadened α-Fe$_2$O$_3$ reflections, particle size and lattice strain of individual phases considering all the reflections cannot be estimated with sufficient accuracy without employing any Rietveld's software based on both structural and microstructure refinements. The rate of mechanosynthesis of Ni–Zn-ferrite is then increased rapidly in course of milling. After 7 h of milling, it seems that all the reflections of starting materials have been disappeared completely and the Ni–Zn-ferrite phase has been grown up completely, because the intensity distribution agrees somewhat well with the standard value (ICDD PDF #08-0234). However, a closer look of XRD pattern of 11 h ball-milled sample reveals the presence of strong reflections of NiO and α-Fe$_2$O$_3$ phases. It indicates that stoichiometric Ni–Zn-ferrite phase is not formed completely even after 11 h of ball milling the stoichiometric powder mixture.

For complete formation of stoichiometric Ni–Zn-ferrite phase, a part of 11 h milled sample is post-annealed at 773 K for different durations. The XRD patterns of post-annealed powders along with 11 h ball-milled powder are shown in Fig. 2 for progressive development of Ni–Zn-ferrite phase in the course of post-annealing durations. It is evident from the figure that all the reflections of NiO and α-Fe$_2$O$_3$ phases completely disappear in the XRD pattern of 1 h post-annealed sample and the intensity distributions of all the Ni–Zn-ferrite reflections agree well with the standard value. It also evident that the peak-broadening does not reduce considerably with increasing post-annealing durations up to 15 h, which signifies that nanocrystalline Ni–Zn-ferrite
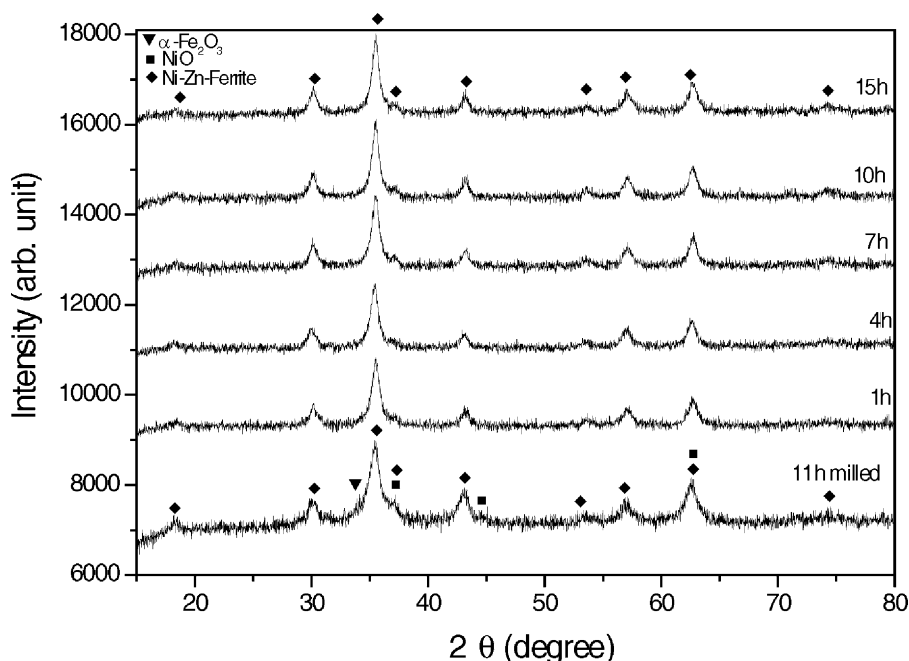
Fig. 2. X-ray powder diffraction patterns of 11 h ball-milled and post-annealed samples.

particles do not grow in size considerably in the course of post-annealing treatment.

In the course of milling, peak-broadening as well as the degree of overlapping of neighboring reflections increase with increasing milling time. To estimate the relative phase abundances, structural changes and microstructure parameters of individual phases, all the unmilled, ball-milled and post-annealed XRD patterns are analyzed employing Rietveld's powder structure and microstructure refinement analysis [16–20]. It is evident from Figs. 1 and 2 that almost all the reflections of these four phases are partially or completely overlapped. Therefore, microstructure parameters and phase content of different phases considering all the symmetry permitted reflections cannot be obtained with sufficient accuracy without adopting the Rietveld's software having both the microstructure and structure refinement facilities. Some of the fitted XRD patterns are shown in Fig. 3 as typical Rietveld's analysis output. The experimental data (I_0; small dots) are fitted well with the refined simulated patterns (I_c; continuous line) because the residue of fitting ($I_0 - I_c$) is negligible and the GoF values for all the fittings lie between 1.07 and 1.25.

Fig. 4 shows the dependence of relative phase abundances of different phases with increasing milling time, milled at a fixed BPMR = 40:1. The content (wt.%) of ZnO phase decreases very rapidly and becomes nil after 1 h of milling. The wt.% of α-Fe$_2$O$_3$ decreases continuously but that of NiO phase very slowly with increasing milling time (Table 1). Significant amounts of NiO ($\sim$7 wt.%) and α-Fe$_2$O$_3$ ($\sim$12 wt.%) phases remain excess even after 11 h of milling. It reveals that within 1 h of milling basically a Zn-ferrite phase has been formed from the ZnO–α-Fe$_2$O$_3$
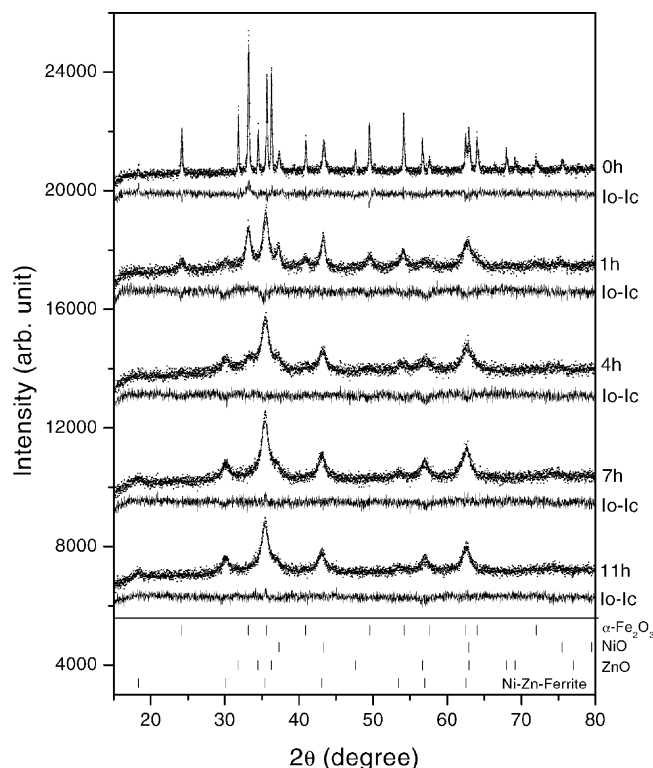
Fig. 3. Observed (·) and calculated (—) X-ray powder diffraction patterns of unmilled and ball-milled samples milled for different durations revealed from Rietveld's powder structure refinement analysis. Peak positions of different phases are shown at the base line as small markers (|).
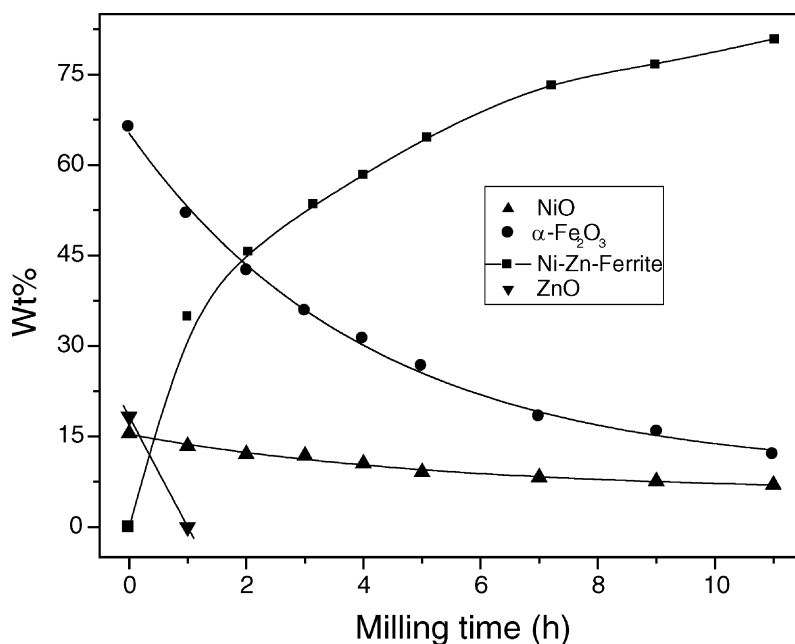
Fig. 4. Variation of phase content (wt.%) of different phases with increasing milling time.

solid solution and a very small amount (∼2 wt.%) of NiO phase diffuses into the Zn-ferrite lattice because at the initial stage of 1 h milling time, the rate of diffusion was very low due to larger crystallite (less reactive) sizes of NiO phase. The amount of ferrite phase increases further due to solid-state diffusion of nanocrystalline NiO and significant amount of α-Fe_2O_3 particles into Zn-ferrite lattice in the course of ball-material–ball/vial collisions. The diffusion rate of NiO is slow. It has been reported earlier [29] that Ni^{2+} ions prefer to occupy the octahedral positions in the spinel lattice. The octahedral positions in Zn-ferrite lattice are already occupied by Fe^{3+} ions and as a result diffusion of Ni^{2+} ions is very slow. However, the formation of NiO–α-Fe_2O_3 solid solution cannot be ruled out. The excess amount of α-Fe_2O_3 and NiO phases may be utilized in formation of stoichiometric Ni–Zn-ferrite phase after a prolong time of milling. The stoichiometric Ni–Zn-ferrite can also be prepared by post-annealing the ball-milled powder at a moderately low temperature for a short duration of time.

The nature of variation of lattice parameters of α-Fe_2O_3, NiO, and Ni–Zn-ferrite phases with increasing milling time is shown in Fig. 5. It is evident from the plots that lattice parameters of α-Fe_2O_3 phase vary nonlinearly as well as anisotropically with increasing milling time. The *a* and *c* values of rhombohedral α-Fe_2O_3 phase increases and decreases, respectively, slowly at the early stage and rapidly up to 5 h of milling and then remain constant till the end of milling (11 h). The increase in *a* value even under compressive stress of ball-material–ball/vial collision may be attributed to the substitution of Fe^{3+} ions (Oct. radius = 0.65 Å) by larger Ni^{2+} ions (Oct. radius = 0.69 Å) preferably along *a*-axis. Similarly, contraction of *c*-axis may also be attributed to the substitution

of Fe^{3+} ions (Oct. radius = 0.65 Å) by smaller Zn^{2+} ions (Oct. radius = 0.60 Å) preferably along *c*-axis (Fig. 5a). Though it was observed earlier [30–32] that high-energy ball milling of α-Fe_2O_3 phase led to formation of different polymorphic iron oxide phases within a very short duration, but surprisingly, in the present study, we did not notice any structural phase transition of α-Fe_2O_3. It indicates that the presence of ZnO and NiO phases prevent the phase transition of α-Fe_2O_3 phase. The variation of lattice parameters with increasing milling time may be further attributed to the accumulation of lattice imperfections in the process of continuous fracture and re-welding of grains under high-energy impact. The lattice parameter of cubic NiO phase increases (Fig. 5b) rapidly up to 5 h of milling and then remains constant till the end of ball milling. The lattice parameter of cubic Ni–Zn-ferrite decreases rapidly up to 5 h of milling and like NiO phase, remains constant till the end of ball milling. As the lattice parameter variations of all the phases do not obey the Vegards law of solid solution (considering lattice deformation by solute addition as deformation induced by increasing milling time), the possibilities of formation of ZnO–α-Fe_2O_3, NiO–α-Fe_2O_3, and ZnO–NiO–α-Fe_2O_3 solid solutions may be ruled out. However, the nanocrystalline Ni–Zn-ferrite is presumed to be formed by different mechanism. Due to high-energy impact, particle sizes of both the NiO and α-Fe_2O_3 phases come down to nanometric order within a very short duration of milling (Table 1). In the course of milling when the nano-sized particles of individual phases come in contact to each other at the time of ball-to-ball and/or ball-to-vial wall collision, nucleation of nanocrystalline Ni–Zn-ferrite particle then takes place by solid-state diffusion between them as both the particle size and collision temperature

Table 1
Microstructure parameters of ball-milled $(NiO + ZnO)$–α-Fe_2O_3 (1:1 mol%) powder revealed from Rietveld's X-ray powder structure refinement method

Milling time (h)	NiO				α-Fe_2O_3					$(Ni–Zn)Fe_2O_4$			
	Lattice parameter (nm)	Particle size (nm)	r.m.s. strain × 10^3, $\langle\varepsilon^2\rangle^{1/2}$	wt.%	Lattice parameter (nm)		Particle size (nm)	r.m.s. strain × 10^3, $\langle\varepsilon^2\rangle^{1/2}$	wt.%	Lattice parameter (nm)	Particle size (nm)	r.m.s. strain × 10^3, $\langle\varepsilon^2\rangle^{1/2}$	wt.%
					a	c							
0	0.4178	24.7	0.1523	15.5	0.5037	1.3754	90.9	0.7871	66.2	0.8399		0	0
1	0.4179	17.7	6.297	13.4	0.5039	1.3732	10.7	3.504	51.9	0.8397	4.2	2.015	34.7
2	0.4181	10.2	6.854	12.1	0.5042	1.3742	8.7	5.898	42.5	0.8396	4.4	2.921	45.4
3	0.4187	9.5	7.528	11.8	0.5046	1.3731	6.7	6.392	35.8	0.8394	4.5	3.015	52.4
4	0.4192	7.5	7.989	10.5	0.5058	1.3616	4.7	6.625	31.1	0.8393	4.5	2.765	58.4
5	0.4197	5.2	8.165	9.1	0.5077	1.3588	3.7	6.981	26.7	0.8392	4.6	3.128	64.2
7	0.4198	5.0	9.524	8.2	0.5108	1.355	3.5	7.568	18.2	0.8393	4.6	2.901	73.6
9	0.4199	4.9	9.701	7.6	0.5115	1.3548	3.6	7.425	15.8	0.8392	4.7	3.018	76.6
11	0.4199	4.9	9.82	7.0	0.5118	1.354	3.5	7.351	12.1	0.8393	4.6	3.128	80.9

Fig. 5. Variation of lattice parameters of: (a) α-Fe$_2$O$_3$ and (b) NiO and Ni–Zn-ferrite phases with increasing milling time.

favors the formation mechanism. The lattice parameter of mechanosynthesized nanocrystalline Ni–Zn-ferrite spinel phases is significantly less (Table 1) in comparison to ICDD (International Centre for Diffraction Data) PDF (Powder Diffraction File) reported (prepared by solid-state reaction at 1523 K of pellets of 0.5 NiO and 0.5 ZnO + α-Fe$_2$O$_3$) value. This mismatch in lattice parameter indicates that the distribution of cations between A and B sites depends on the method of preparation of Ni–Zn-ferrites. This type of lattice mismatch may also arise due to accumulation of significant amount of lattice strain in the ferrite lattice on the progress of milling. Therefore, the increase in lattice parameter of both the phases may be attributed to the influences of both the lattice imperfections as well as continuous redistribution of cations between tetrahedral and octahedral positions.

The nature of variation of particle size (D) and r.m.s. lattice strain $\langle \varepsilon^2 \rangle^{1/2}$ of NiO, α-Fe$_2$O$_3$ and Ni–Zn-ferrite is shown in Fig. 6. Both the particle size and lattice strain of all the phases are found to be isotropic (Table 1). The

particle size of NiO decreases from ~25 to ~17 nm within 1 h ball milling and then decreases slowly with increasing milling time (Fig. 6a). After 7 h of milling, the particle size no longer decreases and remains almost constant till the end of milling. The r.m.s. lattice strain $\langle \varepsilon^2 \rangle^{1/2}$, increases rapidly within 1 h of milling and then slowly in a usual manner with increasing milling time (Fig. 6b). After 7 h of milling, like particle size variation, lattice strain no longer increases and remains almost constant till the end of milling. It signifies that high-energy impact produces enormous amount of lattice imperfections inside the NiO lattice by constant fracturing the grains and the fracturing mechanism of ball milling is obviously more effective when the grains are relatively large. Particle size of the ball-milled α-Fe$_2$O$_3$ phase reduces from ~91 to ~11 nm (Table 1) within 1 h ball milling and then decreases slowly up to 5 h milling and then attains a saturation value of ~4 nm (Fig. 6a). As the particle sizes of both the phases reach almost equal in size (Table 1), it seems that arriving at this critical size particles become

Fig. 6. Variation of: (a) particle size and (b) r.m.s. strain $\langle \varepsilon^2 \rangle^{1/2}$ of NiO, α-Fe$_2$O$_3$ and Ni–Zn-ferrite phases with increasing milling time.

highly vibrant and take part in the formation of Ni–Zn-ferrite nano-particles by individual particle re-welding mechanism. It is also evident from the plot that by increasing the milling time, particle size of α-Fe$_2$O$_3$ cannot be reduced further. It is evident from the plot (Fig. 6b) that the $\langle \varepsilon^2 \rangle^{1/2}$ value increases rapidly within 2 h of milling and then remains almost constant till the end of milling. The variation of particle size of normal Ni–Zn-ferrite spinel phase with increasing milling time is shown in Fig. 6a. From the plot it is clearly evident that normal Ni–Zn-ferrite phase has been formed just after 1 h milling and surprisingly, the particle size ($\sim$4 nm) does not vary significantly with increasing milling time (Table 1). It signifies that partial combination of individual particles of these phases under high-energy

impact initiates the growth of normal spinel particle. The $\langle \varepsilon^2 \rangle^{1/2}$ value of normal spinel lattice increases rapidly up to 2 h of milling and then like particle size, remains almost unchanged till the end of milling (Table 1). The variation indicates towards the following facts: (i) initially normal spinel was formed with a non-stoichiometric composition because starting stoichiometric ratio was not correctly regulated by milling process since significant amounts of α-Fe$_2$O$_3$ and NiO phases were not utilized till the end of 11 h milling. As a result of wrong occupancy of cations in A and B sites, normal spinel lattice became highly strained; (ii) in the course of milling when the particle size attains a critical value ($\sim$4 nm), the grain fracture mechanism of ball milling becomes inoperative and as a result, particle size
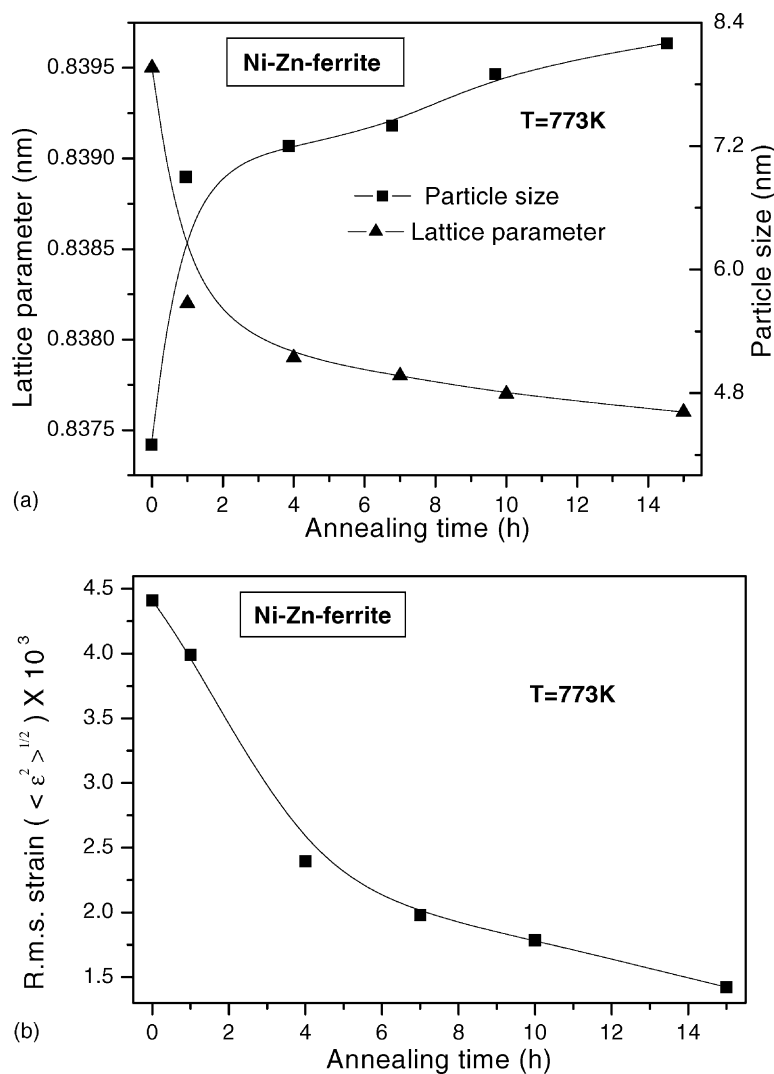
Fig. 7. Variation of: (a) lattice parameter and particle size and (b) r.m.s. strain of Ni–Zn-ferrite phase with increasing post-annealing ($T = 773$ K) time.

as well as lattice strain values of individual phases attain saturation value after a certain period of milling.

The 11 h ball-milled sample was post-annealed at 773 K for 1, 4, 7, 10 and 15 h and XRD pattern of each sample was analyzed by Rietveld's powder structure refinement method (Fig. 2). It is observed that after just 1 h of post-annealing, the residual part of both NiO and α-Fe$_2$O$_3$ phases diffuse completely into the non-stoichiometric Ni–Zn-ferrite lattice and a completely stoichiometric Ni–Zn-ferrite phase has been formed. The lattice parameter of stoichiometric Ni–Zn-ferrite phase decreases rapidly after just 1 h of post-annealing and then remains almost unchanged with increasing post-annealing durations. This implies that excess amount of both NiO and α-Fe$_2$O$_3$ phases diffuse almost completely into the non-stoichiometric ferrite lattice and the redistribution of cations in the tetrahedral and octahedral sites results in contraction of ferrite lattice to get a more complete structure (Fig. 7a). The particle size of the stoichiometric Ni–Zn-ferrite does not increase considerably

(Table 2) as the annealing temperature is only 773 K and the variation of the particle size is shown in Fig. 7a. The lattice strain releases continuously with increasing durations of post-annealing (Fig. 7b) and the nanocrystalline stoichiometric Ni–Zn-ferrite particles become almost strain-free after 15 h of post-annealing at 773 K.

Table 2
Microstructure parameters of post-annealed (NiO+ZnO)–α-Fe$_2$O$_3$ powder (ball-milled for 11 h) revealed from X-ray powder structure refinement method (annealing temperature = 773 K)

Duration of annealing (h)	Lattice parameter (nm)	Particle size (nm)	r.m.s. strain × 10^3, $\langle\varepsilon^2\rangle^{1/2}$
0	0.8395	4.3	4.412
1	0.8382	6.9	3.990
4	0.8379	7.2	2.397
7	0.8378	7.4	1.980
10	0.8377	7.9	1.785
15	0.8.76	8.2	1.423

5. Conclusions

Nanostructured Ni–Zn-ferrite powders have been prepared by high-energy ball milling of stoichiometric mixture of NiO, ZnO and α-Fe$_2$O$_3$ powder within a very short time period. Structural changes of ball-milled NiO, α-Fe$_2$O$_3$, and Ni–Zn-ferrite phases have been investigated by Rietveld's analysis of X-ray powder diffraction data for the first time, to the best of our knowledge. No phase transformation of either NiO or α-Fe$_2$O$_3$ is found throughout the experiment. The quantitative analysis of the XRD data evaluated on the basis of Rietveld's powder structure refinement method yields detailed information about the structure and microstructure of mechanosynthesized nanoscale Ni–Zn-ferrite phase (normal spinel). The accumulation of stored energy during ball milling through repeated fragmentation and re-welding of small grains leads to creation of lattice distortion of Ni–Zn-ferrite phase which is manifested in contraction/expansion of lattice parameter of this phase. The following important observations may be summarized as follows:

(i) Zn-ferrite phase has been formed within 1 h of ball milling.
(ii) Significant excess amounts of both NiO and α-Fe$_2$O$_3$ phases in 11 h ball-milled indicates that the ball-milled prepared sample is a non-stoichiometric ferrite phase.
(iii) Non-stoichiometric ferrite phase has been formed by the combination of nanoparticles of individual phases.
(iv) Post-annealing at 773 K for 15 h leads to the formation of nanocrystalline strain-free Ni–Zn-ferrite particles.

References

[1] P. Ravindernathan, K.C. Patil, J. Mater. Sci. 22 (1987) 3261.
[2] H. Igarash, K. Ohazaki, J. Am. Ceram. Soc. 60 (1997) 51.
[3] A. Goldman, Am. Ceram. Soc. Bull. 63 (1984) 582.
[4] D. Stoppels, J. Mag. Mag. Mater. 160 (1996) 323.
[5] K.H. Lee, D.H. Cho, S.S. Jeung, J. Mater. Sci. Lett. 16 (1997) 83.
[6] C.S. Kim, Y.S. Yi, K.T. Park, H. Namgung, J.G. Lee, J. Appl. Phys. 85 (1999) 5223.
[7] A. Dias, N.D.S. Mohallem, R.L. Moreira, J. Phys. III 6 (1996) 843.
[8] P.S. Anil Kumar, J.J. Shrotri, C.E. Deshpande, S.K. Date, J. Appl. Phys. 81 (1997) 4788.
[9] P. Druska, U. Steinike, V. Sepelak, J. Solid State Chem. 146 (1999) 13.
[10] V. Sepelak, A.Yu. Rogachev, U. Steinike, D.Chr. Uccker, S. Wibmann, K.D. Becker, Acta Crystallogr. Suppl. Issue A 52 (1996) 367.
[11] V. Sepelak, K. Tkacova, V.V. Boldyrev, U. Steinike, Mater. Sci. Forum 783 (1996) 228.
[12] V. Sepelak, A.Yu. Rogachev, U. Steinike, D.Chr. Uccker, F. Krumcich, S. Wibmann, K.D. Becker, Mater. Sci. Forum 139 (1997) 235.
[13] R.O. Sack, M.S. Ghiorso, An internally consistent model for the thermodynamic properties of Fe–Mg titanomagnetite aluminate spinels, Contrib. Miner. Petrol. 106 (1991) 474.
[14] C.N. Chinnasamy, A. Narayanasamy, N. Ponpandian, K. Chattopadhyay, H. Guerault, J.M. Greneche, J. Phys.: Condens. Mat. 12 (2000) 7795.
[15] J.M. Daniels, A. Rosencwaig, Can. J. Phys. 48 (1970) 381.
[16] L. Lutterotti, P. Scardi, P. Maistrelli, J. Appl. Crystallogr. 25 (1992) 459.
[17] L. Lutterotti, MAUD, Version 1.85, 2002. http://www.ing.unitn.it/~luttero/maud.
[18] H.M. Rietveld, Acta Crystallogr. 22 (1967) 151.
[19] H.M. Rietveld, J. Appl. Crystallogr. 2 (1969) 65.
[20] R.A. Young, D.B. Wiles, J. Appl. Crystallogr. 15 (1982) 430.
[21] R.A. Young, The Rietveld Method, Oxford University Press/IUCr, Oxford, 1996, pp. 1–38.
[22] J.G.M. Van Berkum, Ph.D. Thesis, Delft University of Technology, The Netherlands, 1994.
[23] S. Bid, S.K. Pradhan, J. Appl. Crystallogr. 35 (2002) 517.
[24] S. Bid, S.K. Pradhan, Mater. Chem. Phys. 82 (2003) 27.
[25] H. Toraya, J. Appl. Crystallogr. 31 (1998) 333.
[26] H. Toraya, J. Appl. Crystallogr. 33 (2000) 1324.
[27] S. Enzo, G. Fagherazzi, A. Benedetti, S. Polizzi, J. Appl. Crystallogr. 21 (1988) 536.
[28] B.E. Warren, X-ray Diffraction, Addition-Wesley, Reading, MA, 1969, Chapter 13.
[29] S. Adriana Albuquerque, D. Jose Ardisson, A.A. Macedo Waldemar, C.M. Alves Maria, J. Appl. Phys. 87 (2000) 4352.
[30] M. Zdujic, C. Jovalekic, Lj. Karanovic, M. Mitric, D. Poleti, D. Skala, Mater. Sci. Eng. A 245 (1998) 109.
[31] M. Zdujic, C. Jovalekic, Lj. Karanovic, M. Mitric, Mater. Sci. Eng. A 262 (1999) 204.
[32] S. Bid, A. Banerjee, S. Kumar, S.K. Pradhan, U. De, D. Banerjee, J. Alloys Comp. 326 (2000) 292.